

Heat transfer amplification in transitional shock-wave/boundary-layer interactions

J. Lunte* and E. Schülein†

*German Aerospace Center (DLR), Institute of Aerodynamics and Flow Technology,
D-37073 Göttingen, Germany*

Heat flux measurements of transitional shock-wave/boundary-layer interactions (SWBLI) were conducted by quantitative infrared termography. The shock intensity and mutual position of the impingement and transition locations were varied independently. The shock induced Stanton number peaks are maximal for transitional SWBLI and stronger shocks cause higher heat transfer amplification. The highest amplification rates for each shock intensity depend on the transitional state at the impingement location. Weaker shocks require a further developed transitional state at the impingement location for the highest amplification due to less shock induced turbulence. Numerical simulations with the DLR TAU-Code were conducted for the limiting boundary layer cases (laminar & turbulent) and cover the entire experimental parameter study.

Nomenclature

α	deflection angle
\dot{q}_w	heat flux density
γ_{imp}	equivalence of the intermittence factor
κ	heat capacity ratio
Re_1	unit Reynolds number
Re_x	Reynolds number based on the longitudinal coordinate
St	Stanton number
a, b	fit variables
c_f	skin friction coefficient
c_p	specific heat at constant pressure
M	Mach number
p	pressure
r	recovery factor
T	temperature
T_r	recovery temperature
u	streamwise velocity
x, y, z	longitudinal, vertical and spanwise coordinate
y^+	dimensionless wall distance

Subscripts

∞	free stream flow conditions
imp	conditions at the shock impingement location
lam	laminar boundary layer conditions
max	conditions at the maximum of the distribution
tr	conditions at the end of transition location
turb	turbulent boundary layer conditions
w/o	conditions without SWBLI
w	conditions at the wall of the flat plate

*PhD Student, Department of High Speed Configurations, jens.lunte@dlr.de.

†Senior Research Scientist, Department of High Speed Configurations, erich.schuelein@dlr.de, Senior Member AIAA.

x	based on the longitudinal coordinate
0	total flow conditions
1	flow conditions upstream of the impinging shock wave
3	flow conditions downstream of the reflected shock wave

I. Introduction

Shock-wave/boundary-layer interactions (SWBLI) are researched for over 60 years.¹ SWBLI are omnipresent in supersonic flows and influence the structure and properties of the flow tremendously. Big progress in the physical understanding and prediction of flows with SWBLI was achieved in the past decades. Nevertheless, some phenomena like heat transfer amplification or the impact of laminar-to-turbulent transition are still very challenging to predict. The research on SWBLI still continues nowadays due to many applications where SWBLI play an important role.

The design of hypersonic inlets is one of these applications. For an efficient engine the total pressure loss inside the inlet has to be minimized. An optimal pressure recovery is achieved by a fan of ideally isentropic compression waves, leading to exceptionally long inlets with thick boundary layers, which in turn decrease the efficiency. In modern compact inlet designs appropriate pressure recovery levels are provided by a series of oblique shocks reflected repeatedly from the internal walls of the inlet diffuser. This goes along with the occurrence of SWBLI for different states of the boundary layer (laminar, transitional and turbulent). Previous investigations showed that the heat transfer of transitional SWBLI can significantly surpass the heat flux of the laminar or turbulent case.^{2,3} Therefore, the reliable prediction of heat transfer rates including SWBLI in transitional boundary layers is of crucial importance for the inlet design to ensure its structural integrity.

A previous study by Schüle² on transitional SWBLI with a fixed shock intensity revealed a dependency between the shock induced heat flux amplification and the transitional state of the boundary layer at the shock impingement location. A local maximum in the amplification rate occurred for shock impingement locations at transitional boundary layers close to the laminar state.

This study continues the work of Schüle² by determining how the shock intensity influences the heat transfer amplification of transitional SWBLI. Therefore, nominally 2-D shock waves, generated by a wedge under different angle of attacks, impinge on a flat plate. By varying the transition onset and shock impingement locations independently, the boundary layer at the interaction region was systematically altered between the laminar, transitional and turbulent state. The experiments are supplemented by numerical simulations covering the limiting boundary layer cases (laminar and fully turbulent) for the experimental conditions.

II. Experimental Program

II.A. Wind tunnel, test model and test conditions

The experiments were conducted in the Ludwig-Tube Facility DNW-RWG in Göttingen at Mach $M_\infty = 6$ flow conditions. Figure 1 shows a sketch of the DNW-RWG. The test section has a diameter of 0.5 m, large enough to accommodate sufficiently big test models. To achieve different transitional boundary layer states at the shock impingement location, the unit Reynolds number Re_1 was varied between $4 \cdot 10^6 \text{ m}^{-1}$ and $12 \cdot 10^6 \text{ m}^{-1}$ by changing the total pressure p_0 at nearly constant total temperature ($T_0 \approx 550 \text{ K}$). The detailed flow conditions of each shot are reported in table 1. More informations about the capabilities and flow quality of the DNW-RWG can be found in Ref. [4].

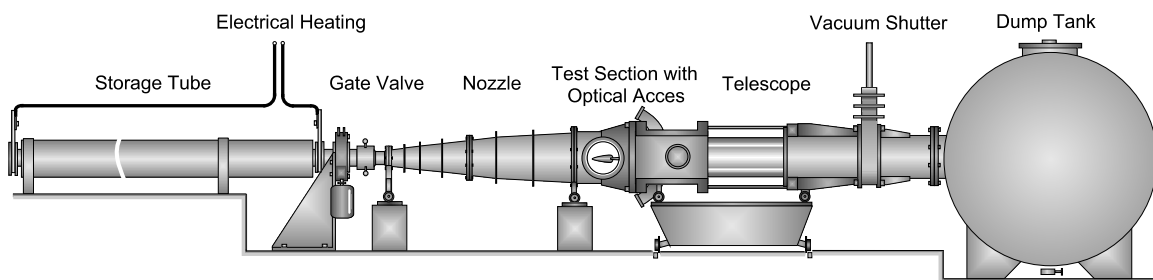


Figure 1. Sketch of the Ludwig-Tube Facility DNW-RWG at DLR Göttingen.

Figure 2 shows the investigated test model. The main flat plate has a sharp leading edge (leading edge radius of the order of $10\text{ }\mu\text{m}$) and is 670 mm in length and 400 mm in width. The plate has a 150 mm wide rectangular cut-out between $x = 126\text{ mm}$ and 526 mm for exchangeable inserts to measure different physical parameters. The shock generator plate (210 mm in length and 300 mm in width) was mounted with deflection angles α of 1, 2 and 3 degrees above the main plate, leading to the corresponding shock intensities of $p_3/p_1 = 1.34, 1.76$ and 2.29 . The vertical height of the shock generator tip above the main plate was 55.6 mm, 58.3 mm and 62.2 mm for the different shock intensities in order to maintain the same non-viscous shock impingement location for all deflection angles. Additionally, the shock generator plate can be mounted at 8 different longitudinal positions. This allows to alternate the position of the non-viscous shock impingement on the flat plate, ranging from $x = 197\text{ mm}$ (Pos. A) to 407 mm (Pos. H) in 30 mm steps. The detailed measurement matrix of the conducted shots is given in table 1.

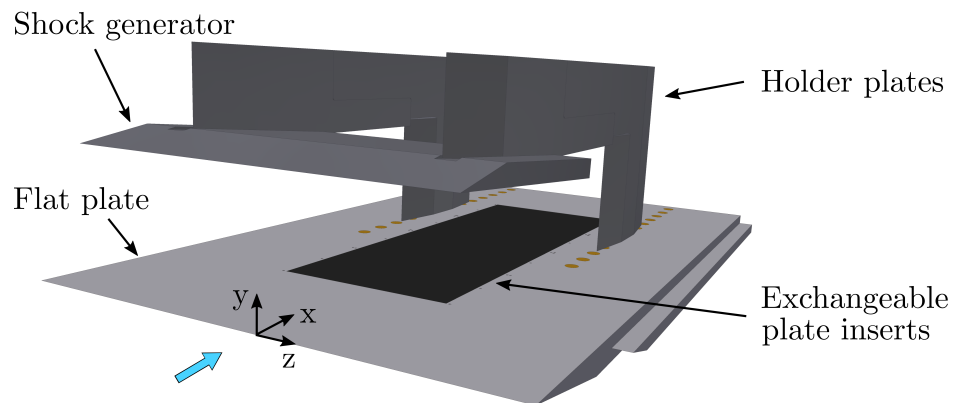


Figure 2. Sketch of the flat plate model with the shock generator plate.

II.B. Quantitative Infrared Thermography (QIRT)

The boundary layer transition and the quantitative heat-flux distributions were measured via infrared thermography. For this purpose, a black Plexiglas® insert with a low thermal conductivity was flush mounted into the cut-out of the flat plate. The insert has a high emissivity due to the mat surface, and the low thermal conductivity minimises the spatial temperature equalisation at the surface as well as in the depth of the insert. These insert properties facilitate measurements of sharp temperature distributions with optimized signal to noise ratios. The surface temperature of the insert was detected by a high speed infrared camera system *IRCAM EQUUS 327kL* at 105 Hz with an exposure time of $100\text{ }\mu\text{s}$ through a Germanium window in the wind tunnel. This camera is based on a 640×512 FPA-sensor, which is sensitive in the spectral range from $8.0\text{ }\mu\text{m}$ to $9.4\text{ }\mu\text{m}$. A sketch of the QIRT measurement setup is shown in Fig. 3.

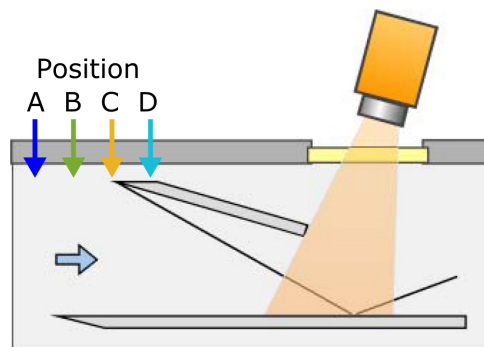


Figure 3. Sketch of the QIRT measurement.

The measured time history of the temperature distributions is analyzed by the in-house developed software *HeatFIT*. For the calculation of the heat flux density \dot{q}_w , the software uses the numerical integration procedure of Fourier's partial differential equation proposed by Cook and Feldermann (Ref. 5, Eq. 83), which is suited for semi-infinite slabs. The program also performs a marker-based 3D-reconstruction of the thermal images and a re-projection of the results onto

the CAD model surface. The reconstruction and identification of the true model coordinates at each pixel enables the spatial averaging of the heat fluxes in span-wise direction, benefited by the two-dimensionality of the main flow.

The span-wise averaged heat-flux distributions are converted to the non-dimensional Stanton number by

$$St = \frac{\dot{q}_w}{\rho_\infty u_\infty c_p (T_r - T_w)}, \quad (1)$$

with the density ρ , velocity u , wall temperature T_w and the specific heat coefficient c_p at constant pressure. The ∞ subscript denotes the freestream conditions of the flow. The recovery temperature T_r is defined as

$$T_r = T_\infty \left(1 + r M_\infty^2 (\kappa - 1) / 2 \right), \quad (2)$$

where κ is the heat capacity ratio. The recovery factor r varies with the boundary layer state. Its value is well known⁶ for laminar and turbulent boundary layers but unknown in the transitional region. For a simplified comparison of the Stanton number between the different investigated states all heat flux densities were scaled with the laminar recovery factor $r = 0.85$. This simplification leads to an artificial increase of the Stanton number for turbulent boundary layers by

$$\frac{T_{r,\text{turb}} - T_w}{T_{r,\text{lam}} - T_w} \approx 1.11. \quad (3)$$

To compare the experimental results with theoretical and numerical solutions, the Stanton number for the turbulent cases are consequently increased by 1.11. Details of the program *HeatFIT* and the analysis of the temperature distributions are given by Schüle².

deflection angle [°]	Pos.	p_0 [bar]	T_0 [K]	Re_1 [10^6 m^{-1}]
no shock	-	5.40	549.65	3.90
no shock	-	5.54	543.55	4.08
no shock	-	8.21	545.15	6.01
no shock	-	8.26	545.15	6.05
no shock	-	10.95	547.65	7.96
no shock	-	11.27	551.75	8.09
no shock	-	13.71	545.15	10.04
no shock	-	13.74	545.95	10.04
no shock	-	16.40	549.35	11.86
no shock	-	16.44	551.05	11.83
3	A	8.19	546.75	5.97
3	A	11.03	552.25	7.91
3	A	13.62	557.15	9.63
3	A	16.51	551.35	11.87
3	B	5.51	542.55	4.07
3	B	8.35	547.55	6.07
3	B	11.08	547.75	8.05
3	B	13.60	554.05	9.70
3	B	16.48	554.15	11.75
3	C	13.92	553.22	9.95
3	C	16.54	555.95	11.73
3	F	5.52	541.55	4.09
3	F	8.26	553.75	5.90
3	F	8.30	551.75	5.96
3	F	11.17	554.15	7.96
3	F	11.12	546.35	8.11
3	F	13.74	547.65	9.99
3	F	16.47	557.15	11.64
2	A	11.16	553.95	7.96
2	A	13.74	552.25	9.85
2	A	16.47	551.86	11.82
2	B	8.39	547.55	6.10
2	B	11.01	560.75	7.70
2	B	13.61	553.85	9.71
2	B	16.48	560.85	11.52

deflection angle [°]	Pos.	p_0 [bar]	T_0 [K]	Re_1 [10^6 m^{-1}]
2	B	16.55	549.05	11.98
2	C	11.11	551.45	7.98
2	C	13.74	551.35	9.88
2	C	16.49	549.95	11.90
2	F	5.47	544.45	4.01
2	F	8.35	547.75	6.07
2	F	11.21	555.15	7.97
2	F	11.15	552.95	7.98
2	F	13.68	551.45	9.83
2	F	16.42	552.15	11.78
1	A	11.19	555.35	7.95
1	A	13.78	549.05	9.97
1	A	16.44	546.85	11.98
1	B	11.12	553.75	7.94
1	B	13.76	555.15	9.78
1	B	16.46	548.15	11.94
1	C	13.78	552.75	9.87
1	C	16.48	555.25	11.71
1	F	8.29	544.45	6.08
1	F	8.29	543.95	6.09
1	F	11.12	549.55	8.04
1	F	11.16	544.95	8.18
1	F	13.79	552.25	9.89
1	F	13.81	546.35	10.08
1	F	16.50	555.55	11.72
1	D	8.31	552.15	5.96
1	D	11.18	553.15	7.99
1	D	11.22	548.15	8.14
1	D	13.81	558.15	9.73
1	D	16.62	557.35	11.74
1	E	8.35	542.65	6.16
1	E	11.19	550.35	8.07
1	E	13.85	550.65	9.98
1	E	16.56	556.55	11.72

Table 1. Measurement matrix.

III. Simulation Setup

Numerical simulations were carried out with the finite volume flow solver DLR TAU-Code.⁷ TAU solves the compressible Reynolds-Averaged Navier-Stokes equations (RANS) on hybrid unstructured grids. A detailed description of TAU and its capabilities considering e.g. turbulence models are given in Ref. [8]. In the current work two dimensional steady RANS simulations were performed, with a Backward Euler Relaxation solver. The equations were spatially discretised by a second order upwind method with a flux splitting scheme (AUSMDV).⁹

Estimations for the thickness of normal shocks lead to values of about 200 nm.¹⁰ The necessary spatial resolution to resolve such small structures surpass the capabilities of modern CFD simulation. Therefore, shock waves have to be simulated on much coarser grids, leading to an extended shock wave thickness in the simulations. In this work, a grid convergence study was conducted with the Menter Shear Stress Transport (SST) turbulence model with a fully turbulent boundary layer and four different grid resolutions were investigated. The computational grid was generated using CENTAURTM. The schematic CFD setup is shown in Fig. 4 for the case of $\alpha = 3^\circ$ and the shock generator mounted at Pos. C. The grid has a relative large (≈ 12 mm) prism layer (region A) to ensure the shock induced separation bubble is calculated in the prism layer even for the extreme cases. Because this work focuses on heat fluxes, the wall distance of the first grid cell y^+ has to be significantly below one^{11,12} to get reliable results. In the current work a value of $y^+ < 0.2$ was used. The tetrahedral part of the grid is divided in regions with different resolutions. In region D the size of the tetrahedral cells is limited to 4 mm and in region C the maximum size is 1 mm. Only region B, containing the impinging shock, was refined in this grid study with the four different grid resolutions 1 mm (coarse), 0.5 mm (medium), 0.2 mm (fine) and 0.1 mm (super fine). The size of the prism cells around the shock impingement location (region A) was adjusted to match the respective grid resolution of region B for a smooth transition of the shock wave from the tetrahedral to the prism cells. For the case of the fine grid resolution 250 prism layers were used with a stretching factor of 1.015. The results of this grid study are shown in Fig. 5 for the skin friction coefficient c_f plotted versus Re_x , because the effects of the grid resolution are best visible for this flow parameter.

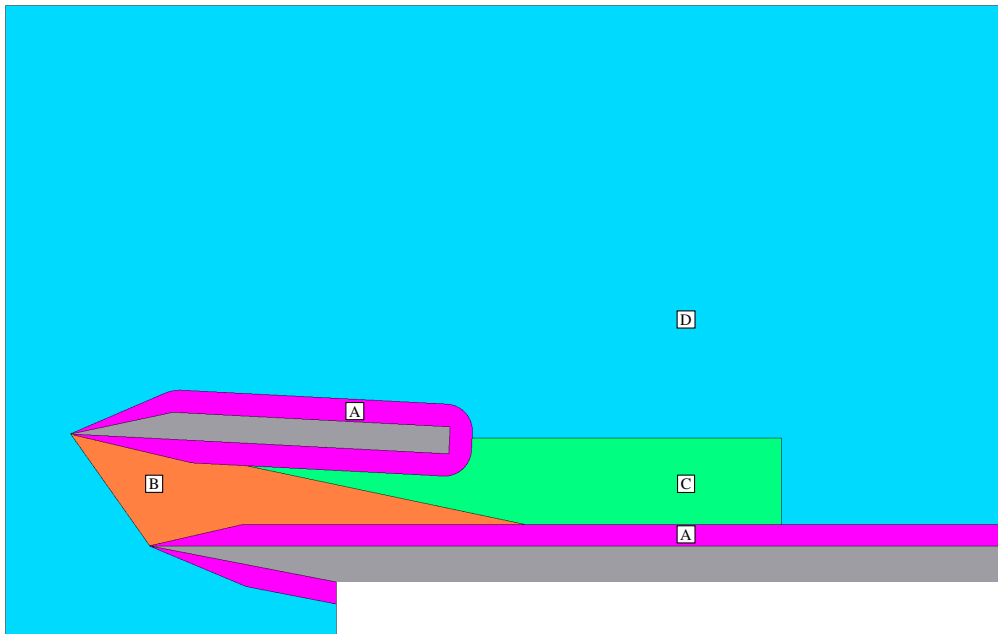


Figure 4. Sketch of the CFD setup for the case of a 3° deflection angle at Pos. C.

The results of all different grid resolutions overlap quite well and show only neglectable differences for most of the flat plate. The only region where major differences occur is immediately upstream of the shock impingement position, which is shown in detail in the inset. All investigated grids negate a flow separation, but the reduction of the skin friction, due to the shock induced pressure rise, gets bigger with increasing grid resolution. The reduction of c_f changes dramatically from the coarse grid to the fine one and only a small difference occurs between the fine and super fine grids. Although the CFD simulation still shows no 100 % grid convergence, the differences between the fine and super fine grids are insignificant, especially if the computational costs are compared to the benefit. Hence, the fine grid resolution has been used in this work, leading to approx. 1.1 million grid points.

Although transitional SWBLI were investigated in the experiments, no simulations with a transitional boundary

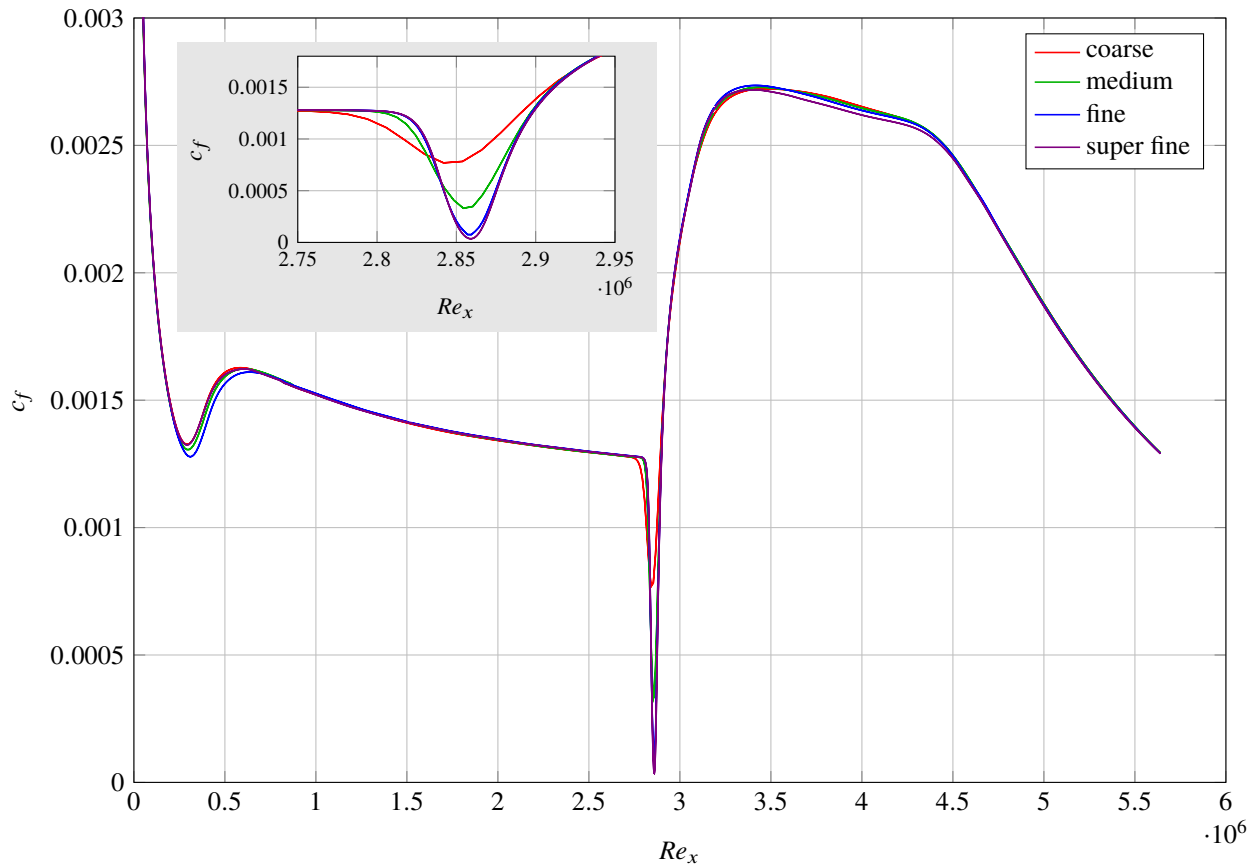


Figure 5. Skin friction coefficient distributions for different grid resolutions on the flat plate with an impinging 3° deflection angle shock wave at Pos. C.

layer were conducted. The correct prediction and description of the laminar-turbulent transition is still a challenging task in modern CFD simulations, especially at high Mach numbers. The transition process at Mach 6 is determined by the second (Mack) mode instability,¹³ which cannot be predicted with the transition models currently implemented in the DLR TAU-Code. Therefore, only simulations of SWBLI with fully laminar and fully turbulent boundary layer states were conducted.

As a next step the influence of the turbulence model was investigated. For that, the fully turbulent flow over the flat plate without a shock generator was simulated with the fine grid resolution for a unit Reynolds number of $12 \cdot 10^6 \text{ m}^{-1}$. The following turbulence models were chosen for the investigation:

- Menter SST model from 1994¹⁴
- Menter SST model from 2003¹⁵
- Standard Spalart-Allmaras model^{16,17}
- Negative Spalart-Allmaras model¹⁷
- Wilcox $k-\omega$ model¹⁸

The Stanton number distributions for each turbulence model are compared with the theoretical curve for the turbulent boundary layer of Van Driest II⁶ in Fig. 6. The Van Driest II correlation (VDII) was used in this paper as the reference Stanton number for the turbulent boundary layer. Additionally, a laminar simulation was conducted and compared with the compressible laminar boundary layer similarity solution.¹⁹

As expected, the laminar boundary layer solution of the DLR TAU-Code overlaps with the theoretical curve. The different versions of the same basic turbulence model exhibit only small deviations. So both Spalart-Allmaras models overlap nearly perfectly, but surpass the VDII Stanton number distribution above $Re_x = 1.2 \cdot 10^6$. The reason for

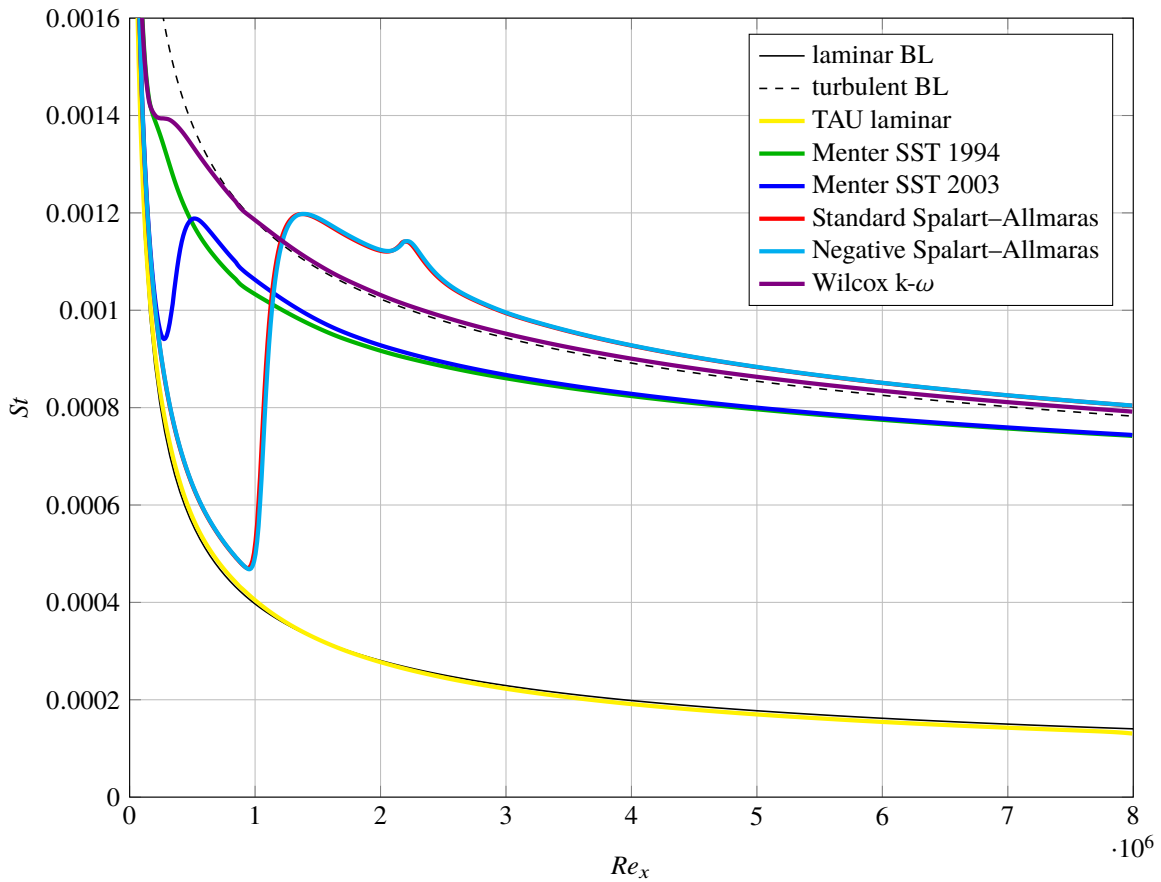


Figure 6. Stanton number distributions of the flat plate for different turbulence models.

the local maximum at $Re_x = 2.2 \cdot 10^6$ is unclear. The Menter SST models differ from each other only upstream of $Re_x = 1.5 \cdot 10^6$ and are below the St curve of VDII over the whole Re_x region. All turbulent models except the Menter SST model from 1994 show a laminar-like behavior before the boundary layer turns turbulent despite a fully turbulent boundary layer was predefined in the settings of the numerical simulation. It is known that turbulence models do not activate directly at the leading edge, but only after a certain distance downstream of the leading edge. The distance depends on the flow properties and was investigated by Rumsey and Spalart.²⁰ As described in section II.B all turbulent Stanton number distributions are corrected by a factor of 1.11. Therefore, the curves of the Spalart-Allmaras models do not overlap with the laminar solution below $Re_x = 1 \cdot 10^6$. For this paper the Wilcox $k-\omega$ model was used for the parameter study, because it agrees best with the theoretical curve of Van Driest II.

Because the requirements for the CFD simulations are difficult, the aim of this work is to analyze to what extend the experimental shock induced heat transfers can be reproduced by the CFD simulations with both limiting boundary layer states (fully laminar and fully turbulent). Therefore, a parameter study was conducted for all combinations of three deflection angles ($1^\circ, 2^\circ$ and 3°), three unit Reynolds numbers ($4 \cdot 10^6 \text{ m}^{-1}$, $8 \cdot 10^6 \text{ m}^{-1}$ and $12 \cdot 10^6 \text{ m}^{-1}$), four shock impingement positions (Pos. A, Pos. C, Pos. E and Pos. G) and two boundary layer states (laminar, turbulent), leading to a total of 72 cases and covering the entire parameter study of the experiments. Additionally, the base flows without a shock interaction were simulated for five unit Reynolds numbers ($4 \cdot 10^6 \text{ m}^{-1}$, $6 \cdot 10^6 \text{ m}^{-1}$, $8 \cdot 10^6 \text{ m}^{-1}$, $10 \cdot 10^6 \text{ m}^{-1}$ and $12 \cdot 10^6 \text{ m}^{-1}$) for both boundary layer states. The flow conditions were selected to match the experiments.

IV. Results and Discussion

IV.A. The basic flow over the flat plate

The heat flux distributions for the basic flow over the flat plate without a SWBLI are shown in Fig. 7 for the investigated unit Reynolds numbers. Again the Van Driest II correlation and the compressible laminar boundary layer similarity

solution are shown in the figure as theoretical reference curves for the turbulent and laminar boundary layers.

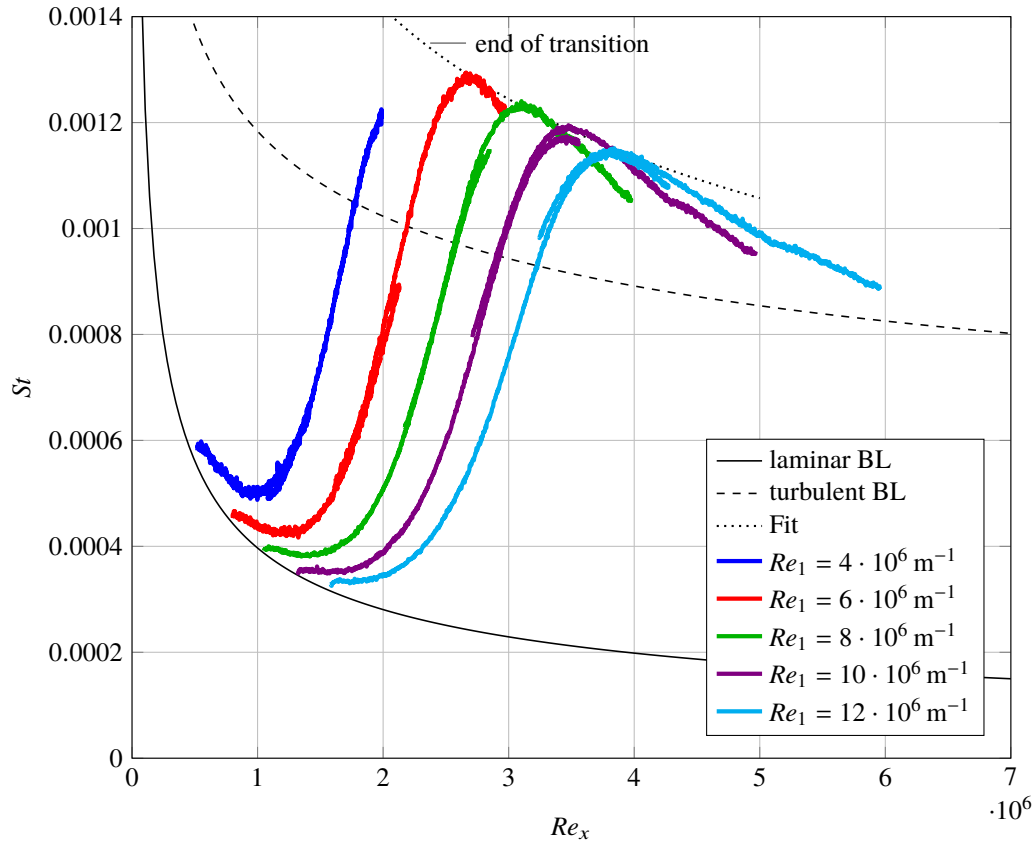


Figure 7. Measured Stanton number distributions for the natural transition on the flat plate without an impinging shock for different unit Reynolds numbers.

All curves start at a laminar boundary layer state, then the heat flux drastically increases, which indicates the transition onset. The heat transfer surpasses the turbulent boundary layer solution of Van Driest II and reaches its maximum. After the maximum, the heat flux relaxes towards the level of the theoretical turbulent boundary layer as indicated by the measurements of the higher unit Reynolds numbers. In the literature the transition Reynolds number Re_{tr} , that indicates the end of transition process, is defined as the Reynolds number at the maximum Stanton number St_{tr} . The unit Reynolds number has a clear effect on the transition process on the flat plate. Low unit Reynolds numbers cause stronger acoustic disturbances of the wind tunnel wall,²¹ which lead to transition locations at lower Reynolds numbers. This effect was observed in different supersonic wind tunnel facilities and Ross²² proposed a correlation for the calculation of Re_{tr} at given wind tunnel conditions. An investigation conducted by Schüle² compared the Re_{tr} dependence on the unit Reynolds number with the correlation of Ross for the Mach 6 conditions at the RWG. The found agreement is excellent and verifies the explanation for the unit Reynolds number effect on Re_{tr} .

To extend the investigated Reynolds number range for each unit Reynolds number, two overlapping regions of the flat plate were observed in separate measurement runs under the same flow conditions. This leads to two curves, which are shifted in Re_x direction. Despite the separate measurement runs, the curves overlay nicely, demonstrating the suitable reproducibility of the measurement technique and the wind tunnel for the conducted parameter study. The statistical error of the Stanton number distributions was determined from 5 measurement runs at the same flow condition, which led to a standard deviation below 2 %.

Each unit Reynolds number has a distinct transition Reynolds number with a corresponding transition Stanton number St_{tr} . A local approximation for St_{tr} is derived by performing a least square fit through the maximum Stanton number of the measured data. The approximated curve is inspired by the laminar boundary layer solution and has the form

$$St_{tr} = a \cdot Re_x^b \quad (4)$$

with the calculated coefficients $a = 0.144$ and $b = -0.319$. The fit is also shown in Fig. 7. This approximation has no deeper physical meaning, but will be used later in this paper for the analysis of the data.

The Stanton number distributions of the CFD simulations for the flat plate without a SWBLI are shown in Fig. 8. The laminar boundary layer solutions agree very well with the theoretical curve for all unit Reynolds numbers. The simulations with the turbulent boundary layer show more differences. The region of the laminar-like behavior (cf. section III) extends as Re_1 decreases until it reaches a plateau at $Re_1 = 6 \cdot 10^6 \text{ m}^{-1}$. These unit Reynolds number effect is known for CFD simulations²⁰ and demonstrate the issues of turbulence models with low Re_1 . On top, the heat flux levels for the two lowest unit Reynolds numbers of $4 \cdot 10^6 \text{ m}^{-1}$ and $6 \cdot 10^6 \text{ m}^{-1}$ are higher than for the other Re_1 . These problems limit the usability of the SWBLI simulation with $Re_1 = 4 \cdot 10^6 \text{ m}^{-1}$ and $6 \cdot 10^6 \text{ m}^{-1}$ drastically.

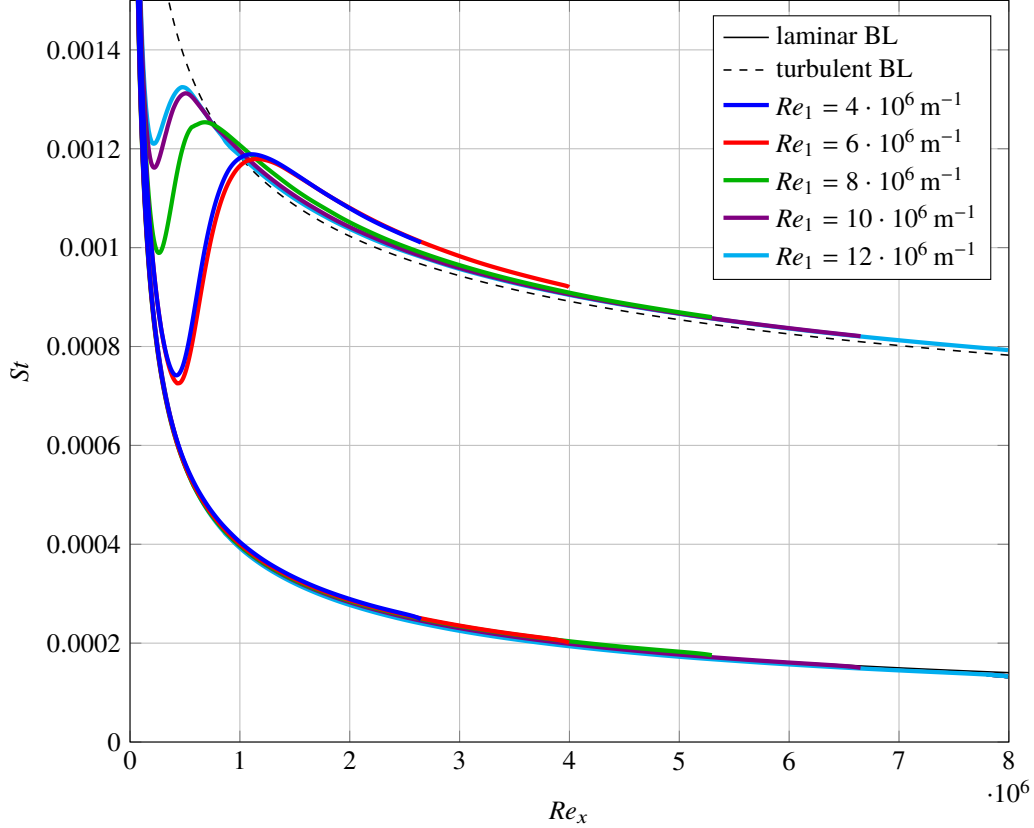


Figure 8. Predicted CFD solutions of the Stanton number distributions for the flat plate without an impinging shock for different unit Reynolds numbers.

IV.B. Transitional SWBLI

A Mach number contour plot of the CFD simulation is given in Fig. 9 for a shock intensity of $p_3/p_1 = 2.29$ and a turbulent boundary layer. The contour plot gives a good impression of the shock interaction and the general flow topology of the investigated setup. The leading edge shock of the flat plate passes below the shock generator and slightly interacts with the generated impinging shock. The SWBLI increases the boundary layer thickness and may cause a separation depending on the shock intensity and boundary layer state. The expansion waves of the shock generator rear increase the Mach number and interact with the reflected shock. Because the length of the shock generator plate is sufficient, the expansion waves impinge on the boundary layer far downstream of the SWBLI region and do not influence the interaction region.

Figure 10 shows the Stanton number distributions for a SWBLI of $p_3/p_1 = 2.29$ with $Re_1 = 12 \cdot 10^6 \text{ m}^{-1}$ at various impingement positions. The fluid is compressed due the impinging and reflected shock wave, which causes an increase in the heat flux density. The effect of the flow compression on the Stanton number can be calculated by the ratio

$$\frac{\rho_3 u_3}{\rho_\infty u_\infty}. \quad (5)$$

The flow compression varies with the shock intensity, leading to compression ratios of $\rho_3 u_3 / (\rho_\infty u_\infty) = 1.22, 1.48$ and 1.77 from the weakest to the strongest investigated shock. The Stanton number distributions without a shock (red

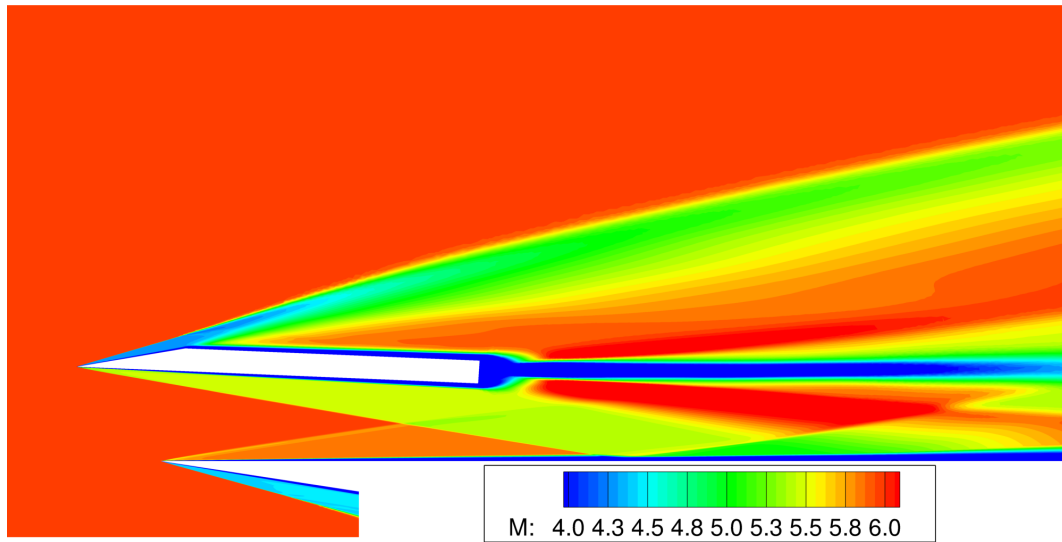


Figure 9. Mach number distribution for a shock generator with a 3° deflection angle and a turbulent boundary layer with $Re_1 = 12 \cdot 10^6 \text{ m}^{-1}$ at Pos. C. The shock waves in the region between the plate and the shock generator are much sharper due to the grid refinement.

lines) are multiplied by the corresponding compression ratio to estimate the increase of the heat flux only due to the compression effect (gray lines). These gray lines titled as "compression" serve as a comparison of the basic heat flux level downstream of the impingement shock.

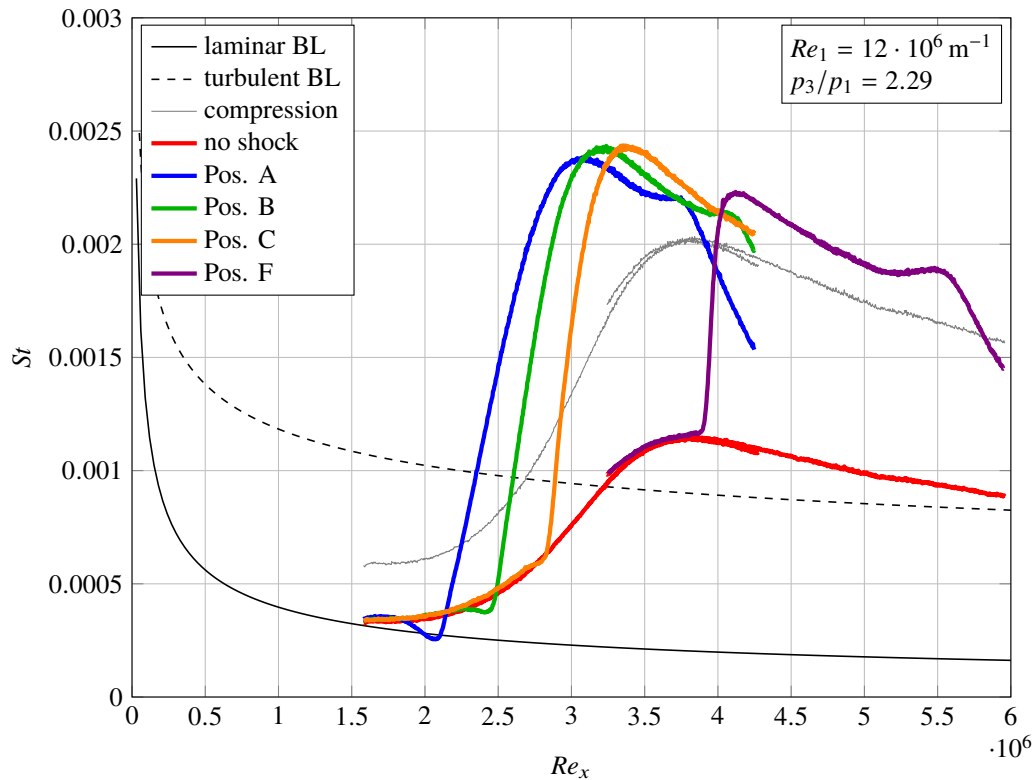


Figure 10. Measured heat flux distributions of SWBLI at various impingement location for a shock intensity of $p_3/p_1 = 2.29$ and $Re_1 = 12 \cdot 10^6 \text{ m}^{-1}$.

The Stanton number distributions with SWBLI in Fig. 10 can be divided in four regions. In the first part, upstream of the interaction, the heat flux values coincide with the basic flow over the flat plate. In the second region, upstream of the shock impingement point, the flow decelerates due to the shock induced pressure rise. Depending on the boundary layer state the flow is delayed or even separated, which decreases the heat transfer. At the same time, the

shock impingement increases the turbulence in the boundary layer, that causes an increase in the heat flux. These two opposing effects influence the Stanton number upstream of the impingement position. Typically, in laminar flows the heat flux reduction due to the delayed flow dominates and leads to large zones of reduced Stanton numbers. But with the ongoing laminar-turbulent transition, the flow can withstand the pressure rise better, which continuously reduces the zone of the locally decreased Stanton number with increasing impingement position (cf. Fig. 10). Finally, the effect of shock induces turbulence dominates and an increase in the Stanton number upstream of the shock impingement can be observed (cf. Pos. F in Fig. 10). The third region starts downstream of the shock impingement. Here, the Stanton number drastically increases due to the compression of the flow and the shock induced turbulence intensification, ending with a heat flux maximum St_{\max} . In the fourth region the shock induced disturbances decline and the Stanton number decreases towards the level of the compression curve. Before the Stanton number reaches this level a second local maximum can be observed (e.g. in Pos. F at $Re_x = 5.5 \cdot 10^6$). The increase in the heat flux is probably caused by another impinging shock wave, which originates from the laminar-turbulent transition at the lower side of the shock generator. This assumption requires further investigations to be confirmed. Downstream of the second maximum the expansion waves, generated at the rear edge of the shock generator, interact with the boundary layer causing a rapid reduction of the heat transfer due to the expansion of the fluid.

Figure 10 shows that the maximum Stanton number value St_{\max} depends on the shock impingement position on the boundary layer. The highest St_{\max} arise in the transitional boundary layer. Another point is the slope of the steep Stanton number rise. The more advanced the transition process is at the impingement location, the steeper develops the St rise. The slope indicates how fast the transition process is accelerated due to the shock induced turbulence. A gentle increase means that the shock induced turbulence is not enough to trigger a direct transition to the turbulent boundary layer, instead the excited disturbances need to grow in the boundary layer to complete the transition.

The Stanton number distributions for the CFD cases of Pos. A and Pos. D are shown in Fig. 11. In both cases the shock intensity was $p_3/p_1 = 2.29$ and the unit Reynolds number was $12 \cdot 10^6 \text{ m}^{-1}$. Additionally, the curves of the numerical solution for the laminar SWBLI and the experimental transitional SWBLI for the corresponding cases are included. This enables a comparison between the experimental transitional SWBLI and the two limiting cases provided by the CFD simulations.

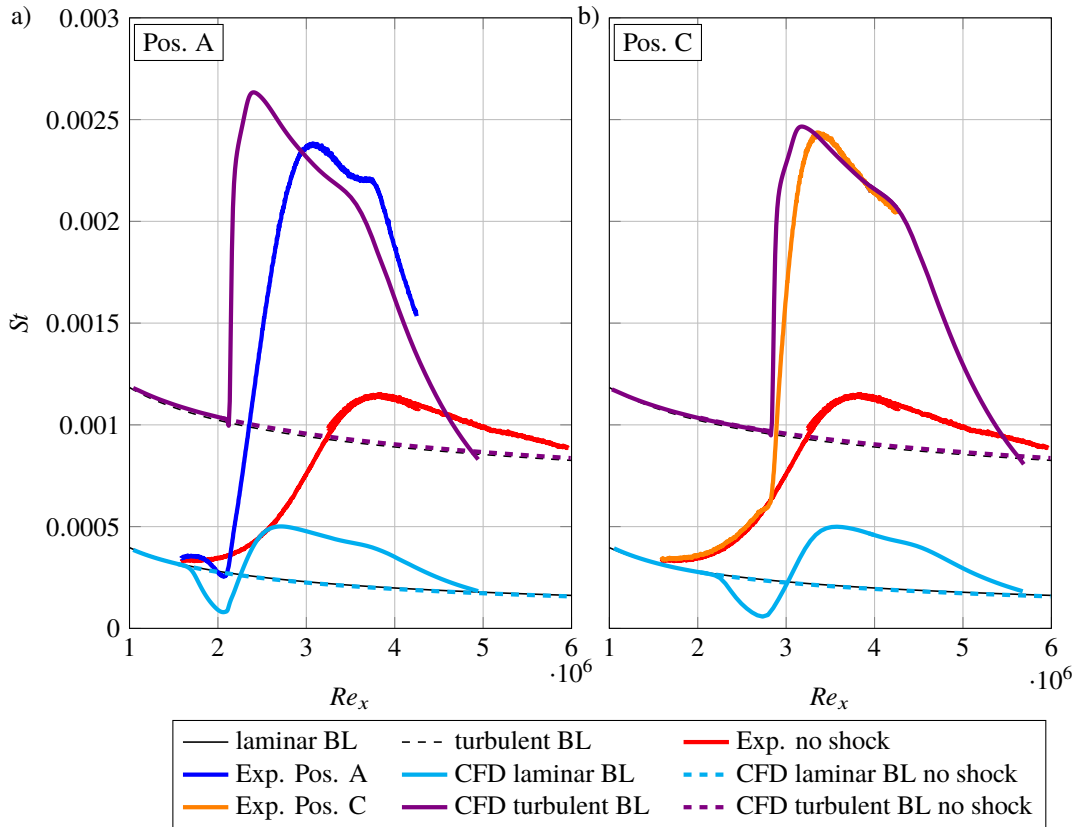


Figure 11. Comparison of the Stanton number distributions between experiment and CFD simulation at two shock impingement locations. In both cases the shock intensity was $p_3/p_1 = 2.29$ and $Re_1 = 12 \cdot 10^6 \text{ m}^{-1}$.

The impact of the boundary layer state on the region of the reduced heat transfer is clearly indicated by the CFD and experimental curves. The laminar boundary layer cannot withstand the pressure rise, which leads to a large flow separation with a significantly reduced heat transfer. For the turbulent CFD simulation the Stanton number is only marginally reduced and the experimental transitional SWBLI lies between these two extremes.

The slope of the Stanton number downstream of the impingement position also varies with the boundary layer state. The slope increases from a relatively small level for the laminar case to a really steep one for the turbulent boundary layer. The transitional SWBLI is again located in between. The effect of the boundary layer state to the slope of the Stanton number rise can also be observed in the experimental data of Fig. 10, where the slope gets gradually steeper with the transitional state at the impingement location.

Another point that can be compared in Fig. 11 is the maximum Stanton number St_{\max} . The Stanton number peak of the turbulent SWBLI simulations decreases if the shock impingement position is further downstream due to the higher boundary layer thickness, while the experiments in Fig. 10 show the highest Stanton number peak at the impingement position B and C. At Pos. C the St_{\max} values of the turbulent SWBLI simulation and the experiment are by chance nearly the same. But if St_{\max} is scaled with the Stanton number of the corresponding undisturbed flow at the same Re_x position, the heat flux amplification of the turbulent CFD simulation significantly surpasses the experimental amplification. This is contradicting with the observations in Fig. 10, where the maximum heat flux amplification is found at transitional SWBLI. The reason for this conflict is an overestimation of the Stanton number peak in the simulations of turbulent SWBLI, which is a known problem.¹¹

After the detailed discussion of only one combination of shock intensity and Re_1 , the next step will be to investigate the effects of the variation of the Re_1 and shock intensity for the experimental transitional SWBLI. Figure 12 compares the influence of the unit Reynolds number on the measured Stanton numbers for transitional SWBLI for the shock intensity of $p_3/p_1 = 2.29$.

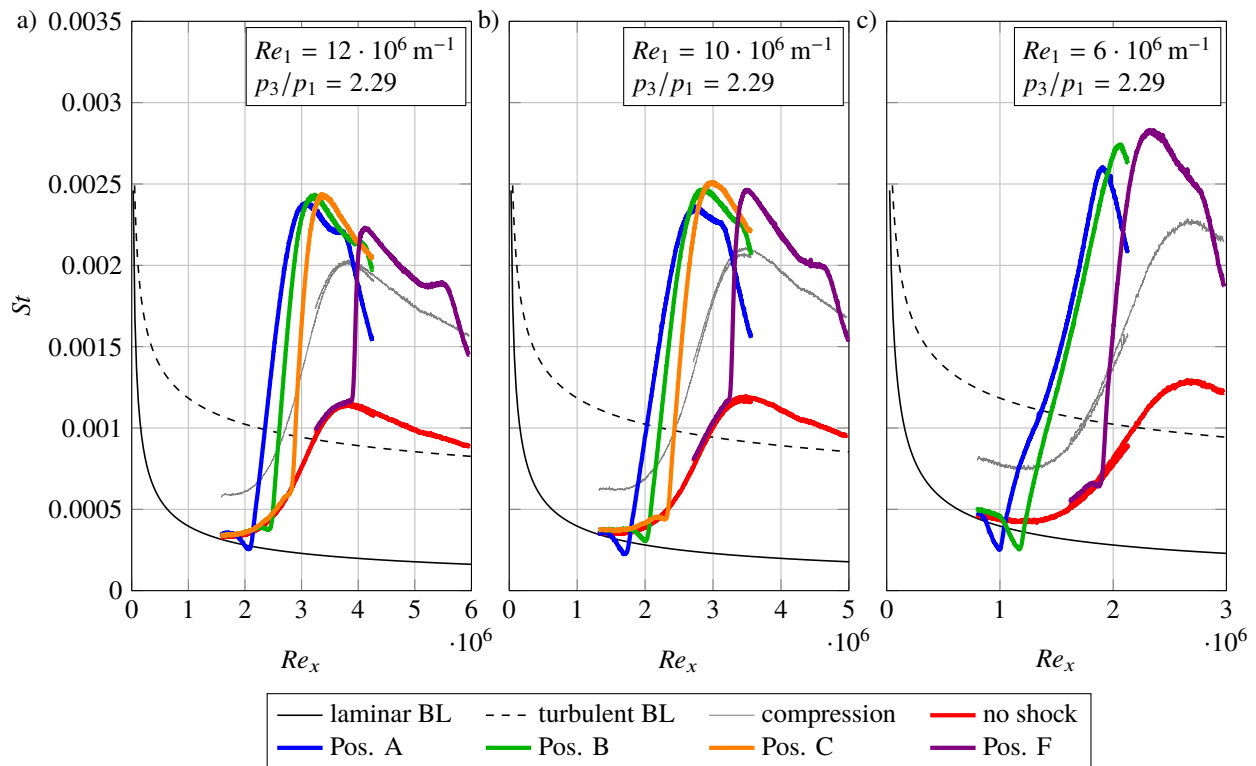


Figure 12. Comparison of the measured Stanton number distributions for different unit Reynolds numbers at a shock intensity of $p_3/p_1 = 2.29$.

As discussed before, a decreasing Re_1 causes an earlier transition due to more acoustic noise with higher Stanton numbers during the transition process (cf. Fig. 7). Because the Stanton numbers of the basic flow are higher, the measured St_{\max} values also increase with decreasing Re_1 . Since the natural transition varies with Re_1 , the boundary layer state changes for a fixed shock impingement position. This can be observed in Fig. 12 for Pos. F. At $Re_1 = 12 \cdot 10^6 \text{ m}^{-1}$ the shock impingement is at the end of the transition, while for $Re_1 = 6 \cdot 10^6 \text{ m}^{-1}$ the shock impinges in the middle of the transition process. Figure 12 also proves that the highest St_{\max} values are not related to a specific shock

impingement position, but are correlated to the transition state at the impingement position as it can be seen for Pos. F. At $Re_1 = 12 \cdot 10^6 \text{ m}^{-1}$ the shock induced St_{\max} value of Pos. F is the lowest, while at $Re_1 = 6 \cdot 10^6 \text{ m}^{-1}$ it surpasses the St_{\max} values of Pos. A and Pos. B. So as Re_1 decreases the highest St_{\max} are generated by a further downstream shock impingement location. The St slope downstream of the shock impingement is also correlated to the transition state at the impingement position.

Figure 13 shows the effect of the shock intensity on the measured St distributions for a fixed unit Reynolds number of $Re_1 = 12 \cdot 10^6 \text{ m}^{-1}$. Weak shocks compress the fluid less and generate less disturbances in the boundary layer. As a direct consequence, the shock induced heat transfer as well as the slope of the Stanton number are decreased. In Figure 13c the different curves proceed no longer next to each other, instead the curves of Pos. A and B even overlap. The shock intensity also influences at which impingement location the highest St_{\max} peak is generated. In Figure 13a the highest St_{\max} values are generated for positions B and C. For the shock intensity of $p_3/p_1 = 1.76$ the highest St_{\max} peaks are induced at Pos. C and for the weakest shock of $p_3/p_1 = 1.34$ at Pos. D.

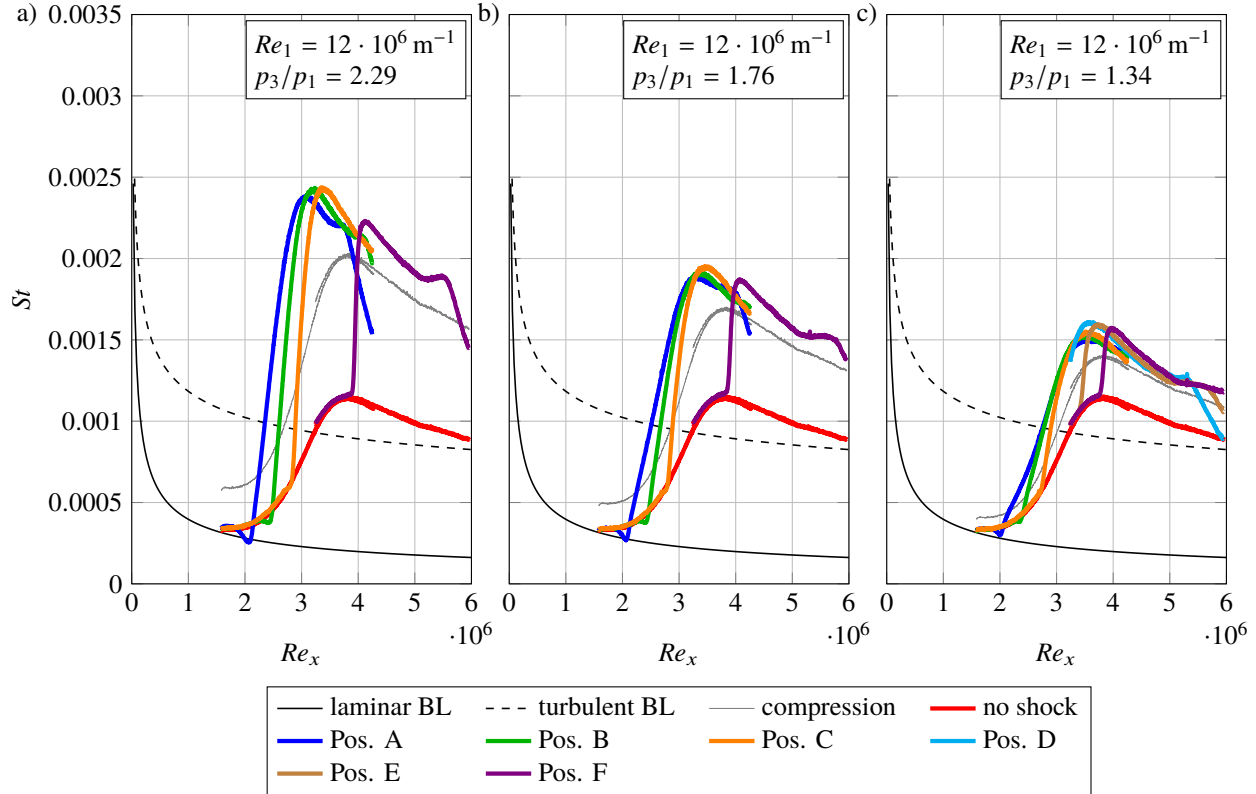


Figure 13. Comparison of the measured Stanton number distributions for different shock intensities at $Re_1 = 12 \cdot 10^6 \text{ m}^{-1}$.

The comparison of Fig. 12 and 13 shows that the maximal heat transfer St_{\max} is influenced by the shock intensity as well as the transition state at the impingement position. This effects can be explained in the following way: the shock introduces additional turbulence in the boundary layer, accelerating the natural transition and leading directly to a turbulent boundary layer. The accelerated transition leads to higher Stanton number peaks St_{\max} , which should be maximal if the introduced turbulence is just enough to cause a direct shift to a turbulent boundary layer. Hence, the weakest SWBLI reaches the highest St_{\max} value (cf. Fig. 13c) only at more downstream location than the stronger shocks. If the transition process is too far advanced at the impingement position (cf. Fig. 13a Pos. F), the heat flux intensification is significantly smaller.

Figure 14 shows the Stanton number distributions of a SWBLI for a shock intensity of $p_3/p_1 = 1.34$ and $Re_1 = 8 \cdot 10^6 \text{ m}^{-1}$. Here, the interaction of a weak shock at a nearly-laminar boundary layer can be seen at Pos. A. The Stanton number first increases due to the flow compression and introduced turbulence, but after the initial rise, the boundary layer stays transitional or even relaxes, resulting in a natural transition with a much slower increase in the Stanton number. Because the shock intensity could not lead to a direct transition of the boundary layer, an overlap between the curves of Pos. A and Pos. B can be seen.

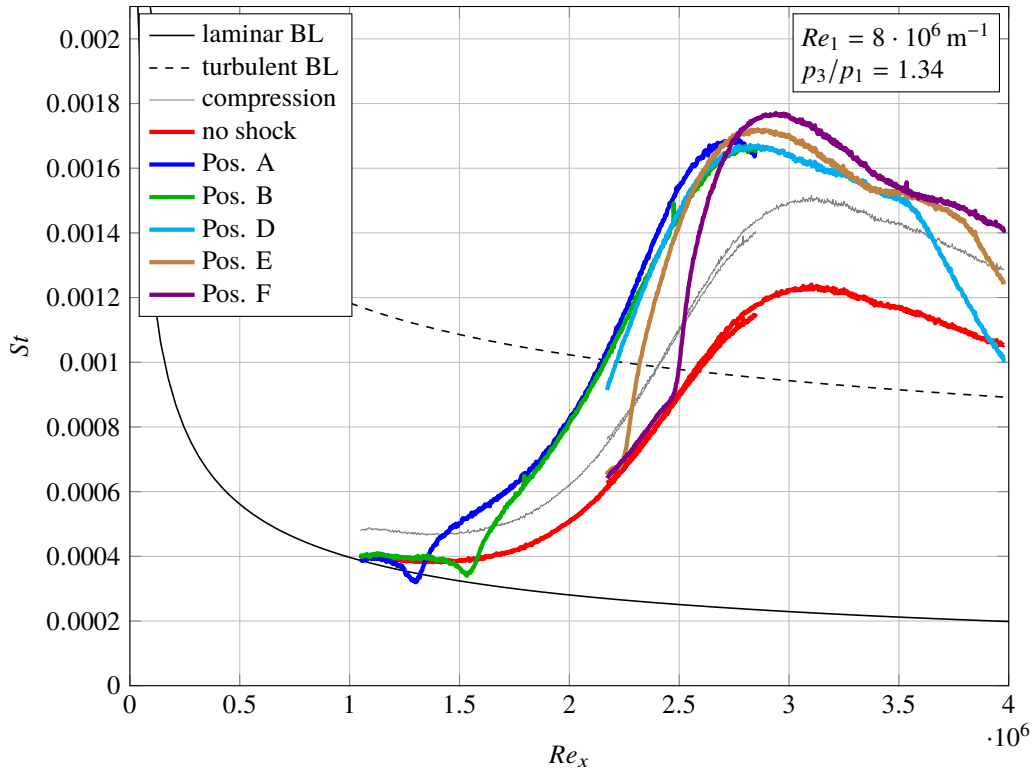


Figure 14. Measured heat flux distributions of SWBLI at various impingement location for a shock intensity of $p_3/p_1 = 1.34$ and $Re_1 = 8 \cdot 10^6 \text{ m}^{-1}$.

IV.C. Heat flux amplification

To quantify the effects of the unit Reynolds number and the shock intensity on the Stanton number peaks, the measurement data are analysed in the following way:² the peak Stanton number St_{\max} is divided by the Stanton number without a SWBLI at the same Re_x as St_{\max} . The relation $St_{\max}/St_{w/o}$ gives the heat transfer amplification due to the SWBLI. The relative position of the shock impingement location within the transition region of the boundary layer will be defined as the intermittence factor γ_{imp} . The intermittence factor γ_{imp} can be derived from the measured Stanton number distributions by

$$\gamma_{\text{imp}} = \frac{St_{\text{imp}} - St_{\text{lam}}}{St_{\text{tr}} - St_{\text{lam}}}, \quad (6)$$

here St_{imp} is the Stanton number of the undisturbed flow at the Reynolds number of the non-viscous shock impingement position Re_{imp} . The transition Stanton number St_{tr} given by equation 4 and the Stanton number of the laminar boundary layer solution St_{lam} are also calculated at Re_{imp} . A sketch of this analysis is provided in the paper of Schüle² and is shown in Fig. 15. This calculation of γ_{imp} indicates the onset of the transition at $\gamma_{\text{imp}} = 0$ and $\gamma_{\text{imp}} = 1$ defines the end of transition.

The results of this analysis are shown for each shock intensity in Fig. 17, 18 and 19 by plotting the the heat flux amplification against the intermittence factor γ_{imp} . For the completeness of this investigation about the influence of the shock intensity on the heat flux amplification, the result of the predecessor paper² with a shock intensity of $p_3/p_1 = 2.95$ is also shown in this paper in Fig. 16. The heat transfer intensification only based on the fluid compression is indicated in the figures and demonstrates that stronger shocks cause higher amplification rates. Clearly, all data points surpass this level due to the additional shock induced turbulence.

The data points for each shock intensity show a collective distribution for all investigated unit Reynolds numbers. Figure 16, 18 and 19 show a locally increased heat flux amplification level. The higher amplification rates correspond to the explanation, that the highest heat fluxes are generated by SWBLI, which introduce just enough turbulence to cause a direct transition to a turbulent boundary layer. For a shock intensity of $p_3/p_1 = 2.95$ the maximum amplification was found at a rather low intermittence factor of $\gamma_{\text{imp}} \approx 0.05$ (cf. Fig. 16). Because of the high disturbance caused by the shock impact, the accelerated transition already happens for nearly-laminar boundary layers.

The strongest investigated shock of the current measurement campaign had a shock intensity of $p_3/p_1 = 2.29$.

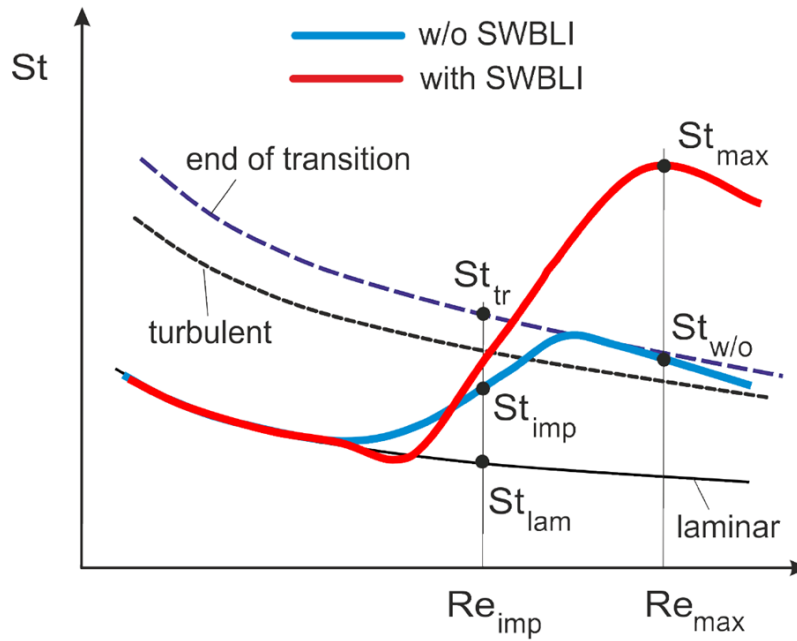


Figure 15. Sketch of the analysis and definition of the parameters.²

For this case the heat flux amplification increases as γ_{imp} decreases from 1 towards 0.1 (Fig. 17). By investigating the amplification rates of the other shock intensities we expect that the $St_{\text{max}}/St_{\text{w/o}}$ values of the $p_3/p_1 = 2.29$ shock intensity should decline for $\gamma_{\text{imp}} < 0.1$. The region of $\gamma_{\text{imp}} < 0.1$ could not be measured because γ_{imp} values near zero can only be reached in low Re_1 flows. At low unit Reynolds numbers the transition process needs an extended length on the flat plate to complete, especially if the shock intensity is not enough to complete the transition directly. On the contrary, the evaluable region on the flat plate is limited by the expansion waves of the shock generator.

The highest amplification rates for the shock intensity of $p_3/p_1 = 1.76$ are between $\gamma_{\text{imp}} \approx 0.2 - 0.3$. For the weakest shock of $p_3/p_1 = 1.34$ (Fig. 19) the amplification rates are tendentially higher at $\gamma_{\text{imp}} \approx 0.7 - 0.9$. The data points of the maximum heat flux amplification show a trend. The weaker the impingement shock, the further devolved must the natural transition be to cause a direct shock induced transition to a turbulent boundary layer.

The data points for the $Re_1 = 6 \cdot 10^6 \text{ m}^{-1}$ case at the investigated shock intensities $p_3/p_1 = 2.29, 1.76$ and 1.34 are above the other data points, which indicates a systematic error. Because all points of the $Re_1 = 6 \cdot 10^6 \text{ m}^{-1}$ case are affected, the reference curve without a SWBLI is probably to low and the reason for the increased $St_{\text{max}}/St_{\text{w/o}}$ values.

The heat flux amplification determined from the numerical parameter study are summarized in table 2. The heat flux amplification rates are averaged over the investigated combinations of unit Reynolds number and shock impingement location. The CFD data points show a correlation with the Reynolds number based on the shock impingement location Re_{imp} . This dependency will not be further analyzed in this paper and the standard deviation of the data points demonstrate that the correlation can be neglected for the current study.

deflection angle	laminar BL	turbulent BL
3°	2.13(5)	2.63(4)
2°	1.70(2)	2.06(2)
1°	1.39(3)	1.58(1)

Table 2. Averaged heat flux amplification rates with standard deviation from the numerical parameter study.

A simple comparison of the CFD amplification rates in table 2 with the experimental data points in Fig. 17, 18 and 19 show a good agreement between the laminar CFD simulations and the experimental data at the limit of $\gamma_{\text{imp}} = 0$. Whereas, the amplification rates for the turbulent boundary layer simulations significantly overpredict the experimental data at $\gamma_{\text{imp}} = 1$. The overprediction of the Stanton number peak in turbulent SWBLI simulations is a known problem,¹¹ that disqualify turbulent SWBLI simulations as a useful limiting case for the current study.

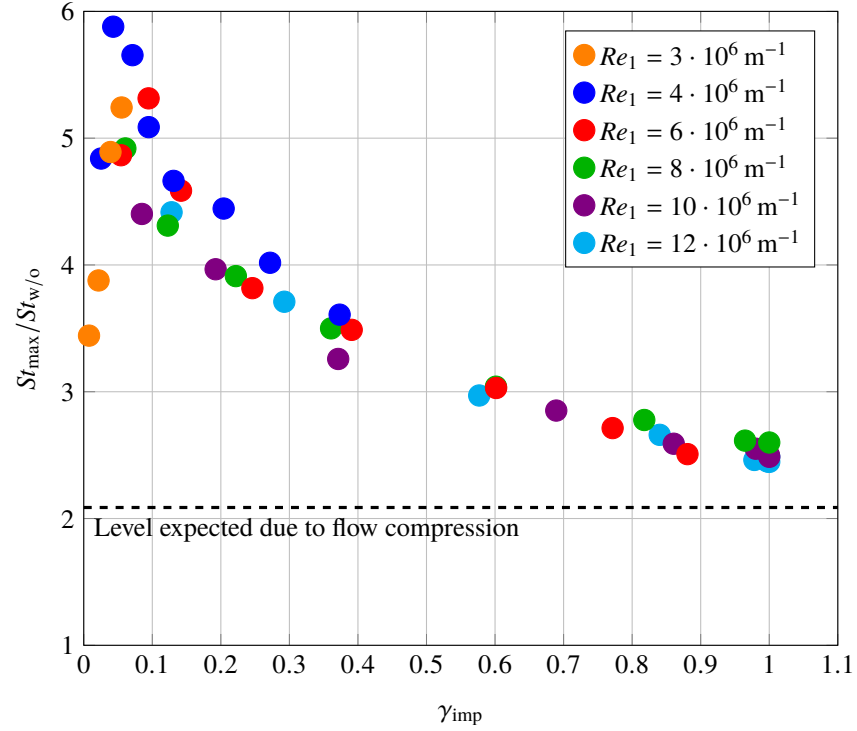


Figure 16. Heat flux amplification against the intermittence factor γ_{imp} for a shock intensity of $p_3/p_1 = 2.95$. Redrawn from Schülein.²

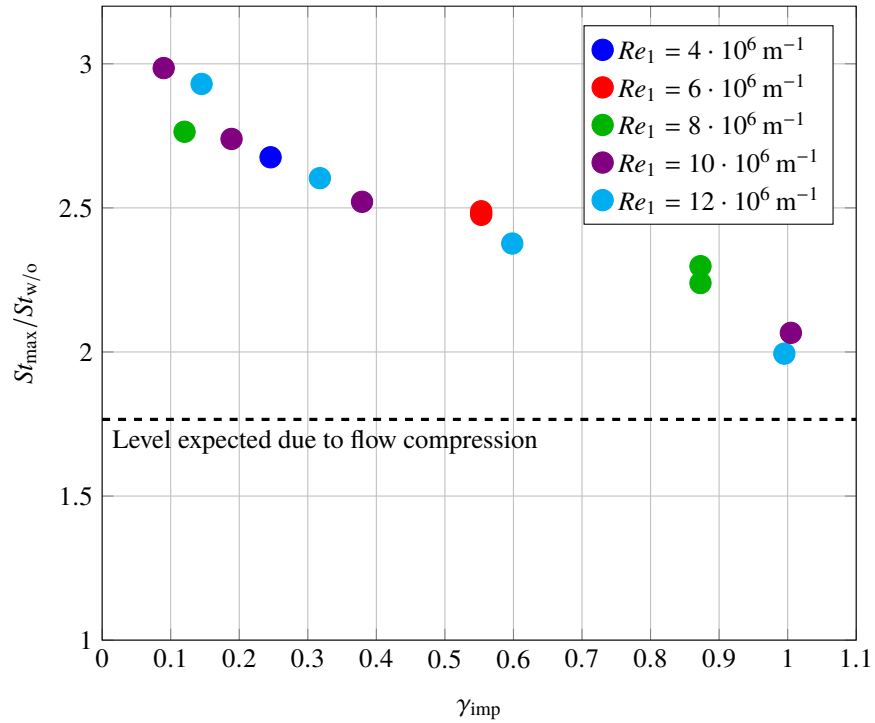


Figure 17. Heat flux amplification against the intermittence factor γ_{imp} for a shock intensity of $p_3/p_1 = 2.29$.

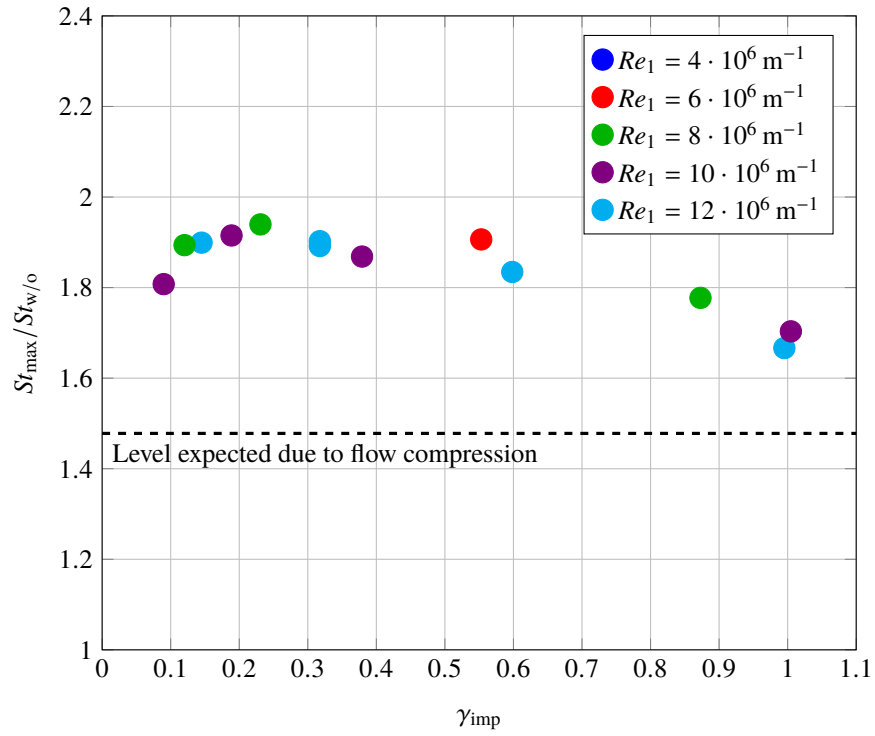


Figure 18. Heat flux amplification against the intermittence factor γ_{imp} for a shock intensity of $p_3/p_1 = 1.76$.

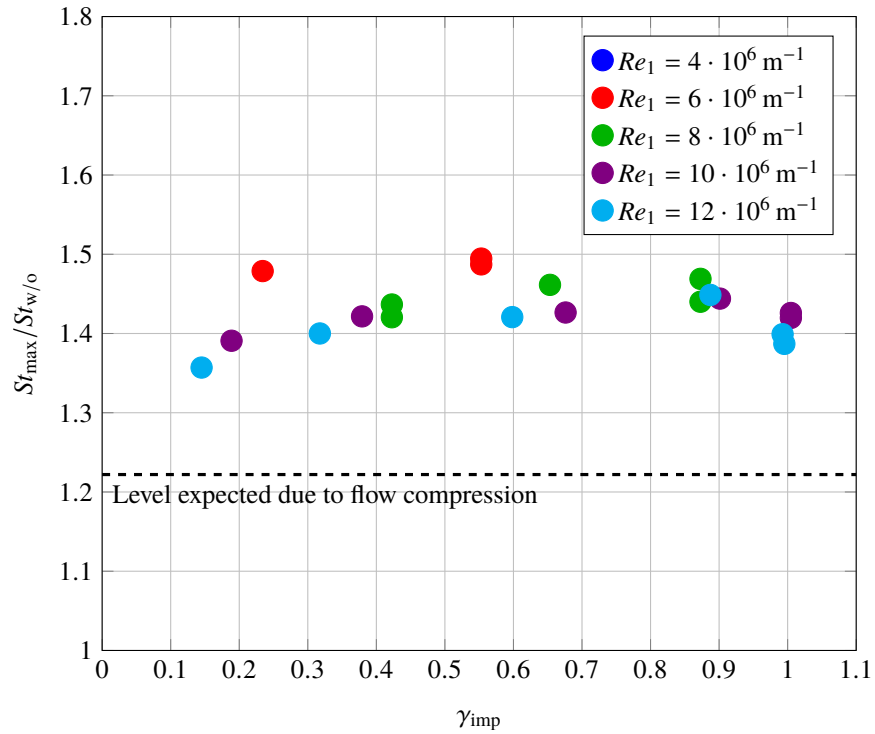


Figure 19. Heat flux amplification against the intermittence factor γ_{imp} for a shock intensity of $p_3/p_1 = 1.34$.

V. Conclusion

Stanton number distributions were acquired on a flat plate with nominally 2-D SWBLI. The boundary layer state at the shock impingement location was varied from laminar to turbulent to investigate the heat flux amplification in transitional SWBLI for three different shock intensities.

The Stanton number distributions for the flat plate without a SWBLI show a clear dependence of the unit Reynolds number on the natural transition location. Stanton number distributions of transitional SWBLI were shown for various combinations of the shock intensity, the unit Reynolds number and the shock impingement location. After an explanation of the general shape of the Stanton number distributions, the effects of each investigated parameter were discussed in detail. The following relations were observed.

The highest Stanton number peaks St_{\max} were generated by transitional SWBLI, but the exact location depends on the combination of transitional state at the impingement location and the shock intensity. If the shock intensity decreases, the highest St_{\max} values were generated by an impingement location at a further developed transitional state.

The observed effects were quantified by introducing a parameter for the heat transfer amplification and a parameter for the transition state at the shock impingement location γ_{imp} . For a fixed shock intensity the measured heat transfer amplification of transitional SWBLI depend on γ_{imp} , leading to locally increased amplification rates at a critical value of γ_{imp} . The shock induced turbulence can lead to a very fast completion of the transition process causing the high heat transfer amplification. It seems that the critical value of γ_{imp} is correlated to the point, where the shock induced turbulence is just enough to trigger this fast transition process. The experimental data yield a trend that the critical value of γ_{imp} increases with decreasing shock intensity.

CFD simulations were performed with the limiting boundary layer states (laminar, turbulent) for the corresponding cases of the experimental parameter study. The challenges of the heat transfer calculations were pointed out for SWBLI at low unit Reynolds numbers. Nonetheless, the simulation results matched the theoretical curves of the flat plate without SWBLI. The CFD solutions with SWBLI were compared with the experiments and showed an ambiguous result. While the CFD simulations describe some tendencies between laminar and turbulent SWBLI correctly, the simulations for the turbulent SWBLI instead are unsuited for a comparison of the heat flux amplification rates with the experimental data.

References

- ¹Dolling, D. S., "Fifty years of shock-wave/boundary-layer interaction research: what next?" *AIAA journal*, Vol. 39, No. 8, 2001, pp. 1517–1531.
- ²Schüle, E., "Effects of laminar-turbulent transition on the shock-wave/boundary-layer interaction," *44th AIAA Fluid Dynamics Conference*, AIAA AVIATION Forum, (AIAA 2014-3332).
- ³Knight, D. D. and Mortazavi, M., "Hypersonic Shock Wave Transitional Boundary Layer Interactions-A Review," *47th AIAA Fluid Dynamics Conference*, AIAA AVIATION Forum, (AIAA 2017-3124).
- ⁴Wagner, A., Schüle, E., Petervari, R., Hannemann, K., Ali, S. R., Cerminara, A., and Sandham, N. D., "Combined free-stream disturbance measurements and receptivity studies in hypersonic wind tunnels by means of a slender wedge probe and direct numerical simulation," *Journal of Fluid Mechanics*, Vol. 842, 2018, pp. 495–531.
- ⁵Schultz, D. L. and Jones, T., "Heat-transfer measurements in short-duration hypersonic facilities." Tech. rep., ADVISORY GROUP FOR AEROSPACE RESEARCH AND DEVELOPMENT PARIS (FRANCE), 1973.
- ⁶Van Driest, E. R., *The problem of aerodynamic heating*, Institute of the Aeronautical Sciences, 1956.
- ⁷Schwaborn, D., Gerhold, T., and Heinrich, R., "The DLR TAU-code: Recent applications in research and industry," *ECCOMAS CFD 2006: Proceedings of the European Conference on Computational Fluid Dynamics*, Delft University of Technology, 2006.
- ⁸"Technical Documentation of the DLR TAU-Code," Tech. Rep. TAU-Code Release 2016.2.0, Deutsches Zentrum für Luft- und Raumfahrt, 2016.
- ⁹Wada, Y. and Liou, M.-S., "A flux splitting scheme with high-resolution and robustness for discontinuities," *32nd Aerospace Sciences Meeting and Exhibit*, 1994, p. 83.
- ¹⁰Granger, R., "Fluid Mechanics," 1985.
- ¹¹Brown, J. L., "Hypersonic shock wave impingement on turbulent boundary layers: Computational analysis and uncertainty," *Journal of Spacecraft and Rockets*, Vol. 50, No. 1, 2013, pp. 96–123.
- ¹²Kovar, A., Hannemann, V., Karl, S., and Schüle, S., "About the Assessment of Heat Flux and Skin Friction of the DLR TAU-code for Turbulent Supersonic Flows," *8th onera-dlr aerospace symposium conference proceedings*, 2007.
- ¹³Mack, L. M., "Boundary-layer linear stability theory," Tech. rep., CALIFORNIA INST OF TECH PASADENA JET PROPULSION LAB, 1984.
- ¹⁴Menter, F. R., "Two-equation eddy-viscosity turbulence models for engineering applications," *AIAA journal*, Vol. 32, No. 8, 1994, pp. 1598–1605.
- ¹⁵Menter, F. R., Kuntz, M., and Langtry, R., "Ten years of industrial experience with the SST turbulence model," *Turbulence, heat and mass transfer*, Vol. 4, No. 1, 2003, pp. 625–632.

- ¹⁶Spalart, P. and Allmaras, S., “A one-equation turbulence model for aerodynamic flows,” *30th aerospace sciences meeting and exhibit*, 1992, p. 439.
- ¹⁷Allmaras, S. R. and Johnson, F. T., “Modifications and clarifications for the implementation of the Spalart-Allmaras turbulence model,” *Seventh international conference on computational fluid dynamics (ICCFD7)*, 2012, pp. 1–11.
- ¹⁸Wilcox, D. C., “Reassessment of the scale-determining equation for advanced turbulence models,” *AIAA journal*, Vol. 26, No. 11, 1988, pp. 1299–1310.
- ¹⁹Sandham, N., Schüle, E., Wagner, A., Willems, S., and Steelant, J., “Transitional shock-wave/boundary-layer interactions in hypersonic flow,” *Journal of Fluid Mechanics*, Vol. 752, 2014, pp. 349–382.
- ²⁰Rumsey, C. L. and Spalart, P. R., “Turbulence model behavior in low Reynolds number regions of aerodynamic flowfields,” *AIAA journal*, Vol. 47, No. 4, 2009, pp. 982–993.
- ²¹Pate, S. R. and Schueler, C., “Radiated aerodynamic noise effects on boundary-layer transition in supersonic and hypersonic wind tunnels,” *AIAA Journal*, Vol. 7, No. 3, 1969, pp. 450–457.
- ²²Ross, R., “A simple formula for flat plate boundary-layer transition in supersonic wind tunnels,” *AIAA Journal*, Vol. 10, No. 3, 1972, pp. 336–337.